The Creep behaviour of Nickel alloy 718 manufactured by Laser Powder Bed Fusion

S. Sanchez[1], G. Gaspard[2], C. J. Hyde[1], I. A. Ashcroft[1], Ravi G. A.[3], A. T. Clare[1 *]

1. University of Nottingham, University Park, Nottingham, Nottinghamshire, NG7 2RD, United Kingdom
2. École Polytechnique Fédérale de Lausanne, Lausanne, Switzerland
3. Renishaw plc., New Mills, Wotton-under-Edge, Gloucestershire, GL12 8JR, United Kingdom

*corresponding author.

Keywords: Laser Powder Bed Fusion; Nickel alloy 718; Creep; Fractography

Abstract

Components manufactured by laser powder bed fusion (LPBF) are limited by their performance for use in critical applications. LPBF materials have microstructural defects, such as suboptimal grain size and morphology, and macroscale anomalies, such as lack of fusion. This results in LPBF components performing below their wrought counterparts for various mechanical properties, such as creep which has seldom been researched. To understand the creep behaviour of LPBF alloy 718, parts were fabricated using different scanning strategies and build orientations and creep tested at 650°C under a 600 MPa load. Heat treatment increased the creep life by a factor of 5, confirming its necessity. The build orientation and stress state were shown to be determining factors in the creep failure mechanisms. The Meander scanning strategy resulted in a 58% increase in creep life compared to the Stripe strategy, due to the detrimental effects of the numerous laser overlapping regions in the Stripe strategy. For a given strategy, a 24% increase in creep life compared to wrought alloy 718 was observed, indicating that LPBF has the potential to surpass wrought material properties. As a result of this work, it is possible to propose build strategies for high temperature creep applications.

1 Introduction

Critical engineering applications, such as turbine blades and discs within aero engines, require components to operate under extreme conditions [1]. Performance of these components is often limited by the mechanical properties of the material and by the geometric design of the part being constrained by conventional manufacturing methods. Additive Manufacturing (AM) offers a potential solution to these limitations and to widening the design envelope into spaces previously unachievable.

It is paramount that any critical component that is designed, manufactured by AM or not, has adequate mechanical properties for safe performance under the application for which it is intended. This can include creep resistance, mechanical and/or thermal fatigue resistance, thermal stability and, where required, low weight/density [2]. Nickel-based superalloys are often used in aero engine applications as they maintain good mechanical properties at elevated temperatures. Indeed, they have the highest temperature and strength combination of all cast and wrought superalloys, which makes them ideal for applications requiring creep resistance. The manufacturing method affects an alloy's grain size and microstructure, which in turn affects its mechanical properties. For example, wrought nickel superalloys are used when high toughness is needed, whilst cast nickel superalloys, which have a larger grain size, are used for high strength and creep resistance in high temperature applications [3]. However, wrought nickel superalloys generally outperform their cast equivalents, making them the industry benchmark. Alloy 718 is one of the best performing nickel superalloys for creep resistance and also shows much greater Laser Powder Bed Fusion (LPBF) manufacturability than many others superalloys [4]. The microstructure of alloy 718 contains a large number of dispersed intermetallics and other phases that modify the alloy's behaviour

by their composition, morphology and location. Alloy 718's main phase, the γ-phase, contains multiple secondary phases which include γ', γ", δ-phase, carbides and intermetallic compounds. The γ' and γ'' phases, FCC Ni_3(Al, Ti) and BCT Ni_3Nb phases, respectively, are the main strengthening phases of alloy 718 and are beneficial to creep-rupture properties. However, between 650°C and 980°C, γ'' transforms into δ-phase, which has been stated as detrimental (decrease in strength) [3] to creep properties. Similarly, carbides can either increase or decrease the alloy's mechanical properties depending on their location, composition and shape. Finally, the Laves phase is an intermetallic phase that embrittles the grain boundaries, leading to unfavourable mechanical and creep properties [5]. The Laves phase may also act as a preferred crack initiation site, resulting in accelerated creep and fatigue crack growth rates [6]. It is thus clear that the microstructure of alloy 718 is the key to its mechanical properties.

At the time of writing, it is not possible for critical components to be manufactured using LPBF alloy 718 as there is a lack of research and understanding about the effect of the LPBF-specific microstructure on its mechanical performance, particularly for high temperature applications where creep may be an issue. Furthermore, due to the fine cellular dendritic microstructure produced by the LPBF process for as-built (AB) material [7], regardless of the use of supports, which can act as heat sink/source [8], the mechanical performance of materials/components, such as ductility, has been found to be inferior to that of cast and wrought materials, especially for creep [9]. Although the creep performance of LPBF alloy 718 has been studied previously, the tests performed were of too short durations for creep mechanisms, such as microvoid coalescence, to have fully taken place (sometimes, less than 2h) [9]. Hence, there is a need for this to be addressed and for the LPBF material to be benchmarked against the wrought equivalent behaviour.

The use of various LPBF process parameters (including laser power, scan speed, hatch spacing, the number of lasers, build orientation, scan strategy and support types), can give rise to different textured microstructures [10], resulting in different mechanical properties [11]. The effect of build orientation on creep performance has been touched on, by comparing the behaviour of horizontally and vertically built specimens [12], however, the effect of building in other orientations has not yet been studied. Similarly, scanning strategies, such as the stripe and meander strategies, and their effect on creep performance have seldom been studied [13].

Another method for enhancing mechanical properties is the application of heat treatments. In industry, almost all high performance metal alloy parts are post-processed using heat treatments as this allows the modification/manipulation of the microstructure through controlled heating and cooling. Following on from the above, it makes sense that by the modification of the microstructure, the mechanical properties can be enhanced. Hence, heat treatments can be used to create an equiaxed microstructure, increase grain size, dissolve detrimental phases (such as Laves) and to form strengthening precipitates at the grain boundaries (such as δ-phase and carbides) [14]. There are many types of heat treatments devised for cast or wrought material, where the effect of the heat treatment depends on the starting microstructure. As the AM starting structure is different to wrought or cast material, typically smaller grained and less precipitation and diffusion, standard heat treatments are not necessarily suited/optimal for LPBF and need to be developed specifically for AM. A typical heat treatment standard used in research papers for LPBF alloy 718 is the AMS 5664 [15], for general mechanical testing of AM components [16], fatigue life [17], thermomechanical fatigue and creep [18]. It has been observed that the creep life of heat treated specimens was enhanced up to 4 times when compared to as-built (AB) counterparts [19], clearly showing the advantages of using heat treatment.

From the literature surveyed it is apparent that there is only limited understanding of the creep performance of LPBF materials due to the low number of papers published and the difficulty to creep test LPBF materials, which resulted in premature failure in some studies. The effect of build parameters and heat treatment on creep performance of LPBF nickel alloys is also poorly understood. It is therefore necessary to evaluate the sensitivity to orientation effects, which gives rise to anisotropic behaviour, scanning strategies and the role of post-build heat treatment. These must be understood if LPBF components are to be deployed in critical applications. In this study, for the first time, the effects of build direction and various scan strategy parameters, on the creep properties of heat treated LPBF alloy 718 are presented and discussed.

2 Methodology

In order to evaluate its creep behaviour, nickel alloy 718 test specimens were manufactured using LPBF, as shown in Figure 1.a. Three different build orientations (0°, 45° and 90°) and two scan strategies (Meander and Stripe) were used and both as-built (AB) and heat-treated (HT) specimens were creep tested until failure. Microscopy and fractography were then undertaken to understand the mechanisms leading to the failure of the material and how the different process parameters affected the creep behaviour.

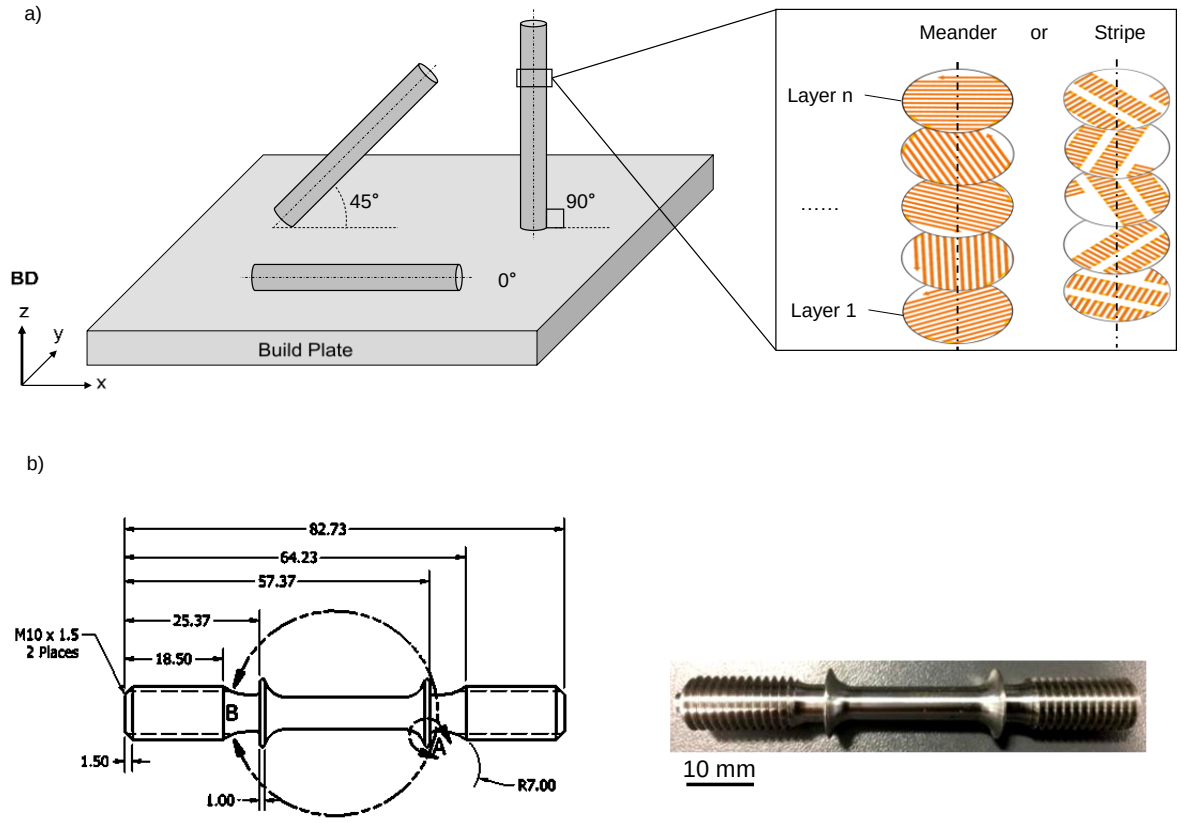

Figure 1: Specimen overview: a) the different parameters investigated: Orientation and scan strategy; b) ASTM E8/E8M [20] uniaxial specimen after turning and grinding. With the Build Direction (BD) indicated.

2.1 Specimen Preparation

Uniaxial cylindrical specimens, were built on a Renishaw© RenAM 500Q quad-laser machine using Renishaw Inconel 718 powder, the composition of which is shown in Table 1. Data from testing AB and heat treated versions of the specimens were compared to that for wrought alloy 718, which was AMS 5662 [21] solution treated material obtained from Carpenter Technology Corporation (Reading, UK).

Table 1: Composition of alloy 718 powder.

Element	Weight %	Element	Weight %
Ni	52.5	Co	0.04
Cr	19.1	C	0.03
Fe	Bal.	Mn	0.02
Nb + Ta	4.89	N	0.01
Mo	3.2	Cu	0.01
Ti	0.86	P	< 0.01
Al	0.42	S	0.001
Si	0.04	B	< 0.001

The specimens were built with the following optimised process parameters (schematically shown in Figure 2) which were developed to reduce build uncertainty and defects caused by phenomenon such as powder spattering [22]:

- Laser Power: 212.5 W;
- Exposure time: 20 µs;
- Hatch point distance: 17 µm;

- Scan Speed: 0.85 m/s;
- Hatch distance: 0.09 mm;
- Stripe offset: -0.2 mm for 90° and 45° specimens and -0.4 mm for 0° specimens.

It should be noted that the 0° Stripe HT specimen has a different Stripe offset as the parameters were not optimised at that time. It was realised that the larger offset would cause over melting, hence this was changed for the build of other specimens and the results and discussion will be presented with this in mind. The reader should also be aware that the heat transfers occurring during LPBF are different for each build orientation and scan strategy, which result in different cooling rates and hence, different microstructures. A summary of all the test cases investigated can be found in Table 2.

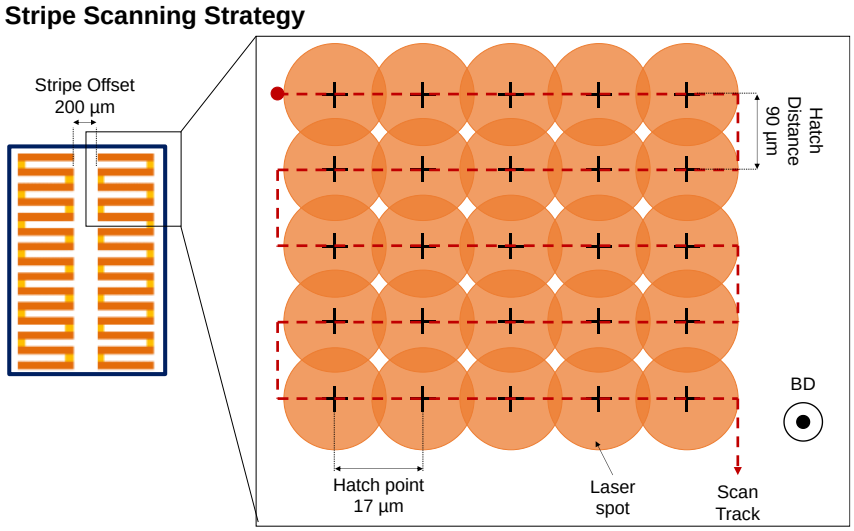

Figure 2: Schematic representation of the Stripe scanning strategy showing the different parameters used. With the Build Direction (BD) indicated.

Table 2: Summary of the different test cases and their process parameters.

Test Case	Orientation	Scan Strategy	Heat Treated
90° Meander AB	90°	Meander	No
90° Meander HT	90°	Meander	Yes
90° Stripe HT	90°	Stripe	Yes
45° Stripe HT	45°	Stripe	Yes
0° Stripe HT	0°	Stripe	Yes
Wrought	-	-	Yes

With the exception of the AB specimen batch, the specimen were solution treated and aged according to the AMS 5662 standard [21] (980°C/1h/Gas quench, 720°C/8h/Furnace Cooling to 620°C/8h/Gas quench). Although this heat treatment was not developed for LPBF material, and hence is not optimised for its starting microstructure, it was used to allow comparison between the LPBF and Wrought specimen performance for the same heat treatment. The specimens were removed from the build plate using Wire Electrical Discharge Machining and the support structures were removed manually. The specimens were then turned using a Tormach Slant-Pro slant lathe to ASTM E8/E8M standard [20] dimensions shown in Figure 1.b, which are recommended for creep testing. Knife edges were included in the specimen geometry to facilitate the use of LVDTs for the measurement of specimen extension. The specimen gauge length of 22 mm was then ground using a P46 grit aluminium oxide grinding wheel mounted on a Jones & Shipman 1302 cylindrical grinder in order to obtain a Ra=0.3 µm surface finish, which plays a major role in creep life.

2.2 Creep Test Procedure

Creep testing was undertaken at 600 MPa and 650°C, according to the ASTM E139 standard [23] using a Denison constant load creep machine (T45A3), which outputs time and extensometer voltage (1 V = 1 mm). A Mathworks (Natick, Massachusetts, USA) commercial software, matlab, and its curve fitting toolbox, which uses regression, interpolation and smoothing to fit curves to data, was used to reduce the noise in the outputted data. Contact thermocouples attached at the top, centre and bottom of the specimen gauge length were used to monitor the temperature uniformity of the furnace. Each test case was repeated 3 times.

2.3 Microstructural Analysis

A Philips XL30 Scanning Electron Microscope (SEM) was used to analyse the specimen fracture surfaces, sections just below the fracture surfaces and reference cubes (from the same build as the creep specimens). An Energy Dispersive X-Ray Spectroscopy (EDS) system by Oxford Instruments (Abingdon, UK) was used in conjunction with the SEM system to perform chemical characterisation of the material and its different phases by using Point & ID in the INCA software by ETAS (Stuttgart, Germany). A Jeol JSM-7100F Electron BackScatter Diffraction (EBSD) was also used to investigate the effect of processing parameters on the crystallography from the reference cubes. An Alicona G5 Infinite Focus, focus variation microscope from Alicona Imaging GmbH (Raaba, Austria), was used to image 3D maps of the tested specimen fracture surfaces. Specimens were cut with a silicon carbide disk and mounted in conductive resin (Metrep Ltd (Coventry, UK) Conducto-Mount) then polished following the recommended Buehler procedure for Ni-based superalloys [24]. Images were processed with ImageJ, an open source image processing programme developed by the National Institutes of Health and the Laboratory for Optical and Computational Instrumentation (University of Wisconsin, Wisconsin, USA), where the precipitate density was obtained using the maximum entropy threshold and the density was given as percentage area (%Area). The precipitate density was found in the planes perpendicular and parallel to the loading direction and averaged. A similar process was used to obtain the %Area of cracks and damage in the fractured specimen. MountainsMaps, a commercial software by Digital Surf (Besançon, France) was used to process the Alicona scans of the fracture surfaces. The HKL Channel 5 software by Oxford Instruments (Abingdon, UK) was used to remove noise in the EBSD scans, plot Inverse Pole Figures and to obtain the grain size, which will be given as an area rather than a diameter, in order for a grain size comparison to be made, due to the elongated aspect of LPBF grains. The standard error, obtained from the standard deviation is indicated for all measurements and results.

3 Results

This section presents the results of the microstructure, the creep tests and fractography investigations for all the specimens listed in Table 2. A detailed discussion of the effects of the various processing parameters on the microstructure of the LPBF alloy 718 and how these result in the observed creep test results is presented in Section 4.

3.1 Microstructure of LPBF specimens

The microstructure of the specimens before and after heat treatment were compared to understand its effect on creep performance and explain the differences in creep behaviour for the different test cases described in Section 3.2.

3.1.1 Grain structure

LPBF usually results in an anisotropic microstructure, with elongated columnar grains oriented in the build direction [25] caused by the remelting of subsequent layers. Indeed, Figure 3 shows that all specimens had elongated grains in the build direction and a more equiaxed microstructure perpendicular to the build direction. This is caused by the cooling gradients towards the substrate, which lead to the directional cooling of grains opposite of the cooling direction (and parallel to the build direction) [26]. The elongated columnar grains, as seen from the plane normal to the build direction, look like equiaxed grains. On that plane, some lines of small equiaxed grains (≤ 150 μm^2) can also be observed, which correspond to laser overlap regions since they are on average roughly 18 μm in width, which corresponds to the 20 μm Stripe offset, and about 77 ± 10 μm apart, which is close to the 90 μm hatch spacing. Whereas the heat treated LPBF specimens had partially recrystallized grains, the grains in AB specimens had ill-defined boundaries and sub-micron sized cell structures (Figure 3.a-a''), similar

to results seen in other studies [27]. Compared to the LPBF specimens, wrought specimens had an equiaxed microstructure in all planes of view, as shown in Figure 3.f-f''. Furthermore, despite having similar processing parameters, the LPBF specimens showed differences in grain size, as shown in Table 3. It can be observed that the heat treated Wrought alloy 718 has significantly smaller grains than the LPBF specimens. The 45° Stripe HT specimen had the largest grains and surprisingly, 90° Meander HT specimen had the smallest, lower than its AB counterpart (see section 4.1.1 for a discussion of these results).

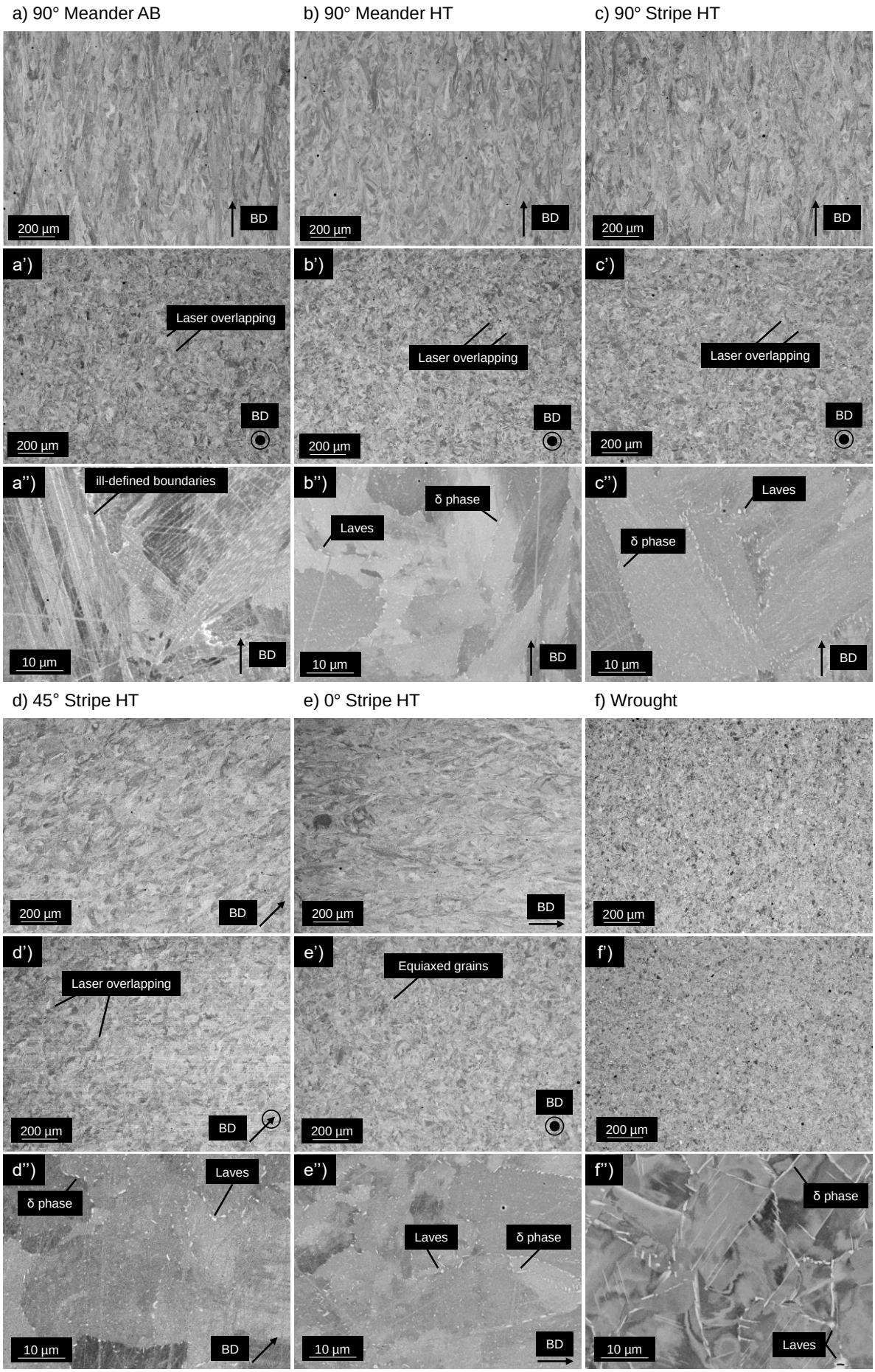
a) 90° Meander AB
b) 90° Meander HT
c) 90° Stripe HT
200 µm
BD
a')
b')
c')
Laser overlapping
a'')
b'')
c'')
ill-defined boundaries
δ phase
Laves
10 µm
d) 45° Stripe HT
e) 0° Stripe HT
f) Wrought
d')
e')
f')
Equiaxed grains
d'')
e'')
f'')

Figure 3: SEM images of the microstructure for the different test cases, showing grain morphology and precipitates. a) - a'') 90° Meander AB; b) - b'') 90° Meander HT; c) - c'') 90° Stripe HT; d) - d'') 45° Stripe HT; e) - e'') 0° Stripe HT; f) - f'') Wrought alloy 718. All images oriented parallel to the loading direction, perpendicular to the loading direction and at a higher magnification to show precipitates, with the Build Direction (BD) indicated. This shows that elongated grains are present along the build direction for all LPBF samples and equiaxed grains with laser overlapping areas (lines of small equiaxed grains), perpendicular to the build direction. Wrought samples, on the other hand, have equiaxed grains in both planes and large precipitates at the grain boundaries.

Table 3: Average grain size and precipitate density for the different test cases.

Sample	Wrought	90° Meander AB	90° Meander HT	90° Stripe HT	45° Stripe HT	0° Stripe HT
Average Grain size (μm^2)	82 ± 2.45	193 ± 19.61	129 ± 12.8	156 ± 9.15	287 ± 35.23	196 ± 18.74
Average Precipitate density (%Area)	2.97 ± 0.15	0 ± 0.00	0.24 ± 0.15	0.43 ± 0.15	0.33 ± 0.15	0.33 ± 0.15

3.1.2 Precipitates

Heat treatment results in the precipitation of strengthening precipitates such as γ'' and δ [28], as well as the dissolution of detrimental phases such as the Laves phase. Since AB specimens were not heat treated, inter-dendritic Laves phases and carbides were present. They were also observed in other studies with different powder compositions [29] and build orientations [27]. In the heat treated specimens, δ precipitates were present at the grain boundaries (Figure 3.b'', c'', d'', e''). This was confirmed by their needle shape and elemental composition (Table 4), similar to theory and other works, as shown by Xu et al. [19]. Furthermore, the δ phase precipitates were oriented in line with the build direction due to the elongated grains in that direction, which may have affected the creep rate and failure mode. Furthermore, the size, quantity and orientation of the δ particles varied for each test case (Table 3). Wrought alloy 718 had the highest δ precipitate density, almost 100 times larger than the closest LPBF specimen (90° Stripe HT) while the 90° Meander HT specimen had the lowest concentration of δ precipitates.

Table 4: EDS analysis of a δ particle on the grain boundaries compared to the γ matrix. (All values within ± 2 wt%)

	Elemental Composition (wt%)	
Elements	**γ matrix**	**δ particle**
Al	0.53	0.36
Ti	1.03	1.72
Cr	19.13	11.82
Fe	18.54	11.33
Ni	52.04	56.43
Nb	5.63	16.12
Mo	3.10	2.22

3.1.3 Crystallographic orientation

Figure 4 shows the EBSD maps oriented according to the loading direction (with individual build directions specified for the different cases) while the inverse pole figures were processed so that the Z direction corresponds to the build direction of the different specimens (except for the 45° Stripe HT specimen, whose Z direction corresponds to the loading direction). 90° Meander AB specimens had a very strong 001 crystallographic orientation parallel to the build direction, which was observed in other studies [30], and a slight texture perpendicular to the build direction (Figure 4.a). The EBSD map clearly shows elongated and ill-defined grains in the build direction as well (Figure 4.a). In comparison, the 90° Meander HT specimen had a less strong 001

texture in the build direction and more defined and recrystallised grains although melt pools were still apparent (Figure 4.b), which shows that there is a reduction in texture after heat treatment, which is in agreement with other studies [31]. The 90° Stripe HT specimen had a similar microstructure to the 90° Meander HT, with elongated grains in the build direction, but a stronger 001 texture parallel to the build direction than both AB and HT 90° Meander specimens (Figure 4.c). In another study however, Newell et al. found that, Stripe specimens retained less texture than Meander equivalents [31], which was not the case in the present work. The present findings show that the Meander scan strategy results in less texture than Stripe scan strategies, regardless of heat treatment. Furthermore, the 45° Stripe HT specimen (which is oriented so that Z is the loading direction) presented a 111 texture slightly perpendicular to the loading direction - which likely corresponds to its build direction - and grains elongated at about 30° to 45° from the loading direction (Figure 4.d), which corresponds to the build direction of the specimen. The 0° Stripe HT specimen, similarly to the 90° Meander specimens, had a 001 texture in line with its build direction (Figure 4.e). Finally, the wrought specimen clearly presented small equiaxed grains, compared to the LPBF specimens as well a slight texture in the 111 direction (Figure 4.f), which probably corresponds to the extrusion direction. Overall, most LPBF samples had a 001 texture in line with their build direction as well as elongated grains. These textures and grain orientations have been shown to result in anisotropic mechanical properties, such as yield strength [32], and these textures likely affected the creep performance of the specimens. The creep behaviour of the specimens will now be presented, followed by fractography, which is required to obtain a further understanding of the creep mechanisms causing failure.

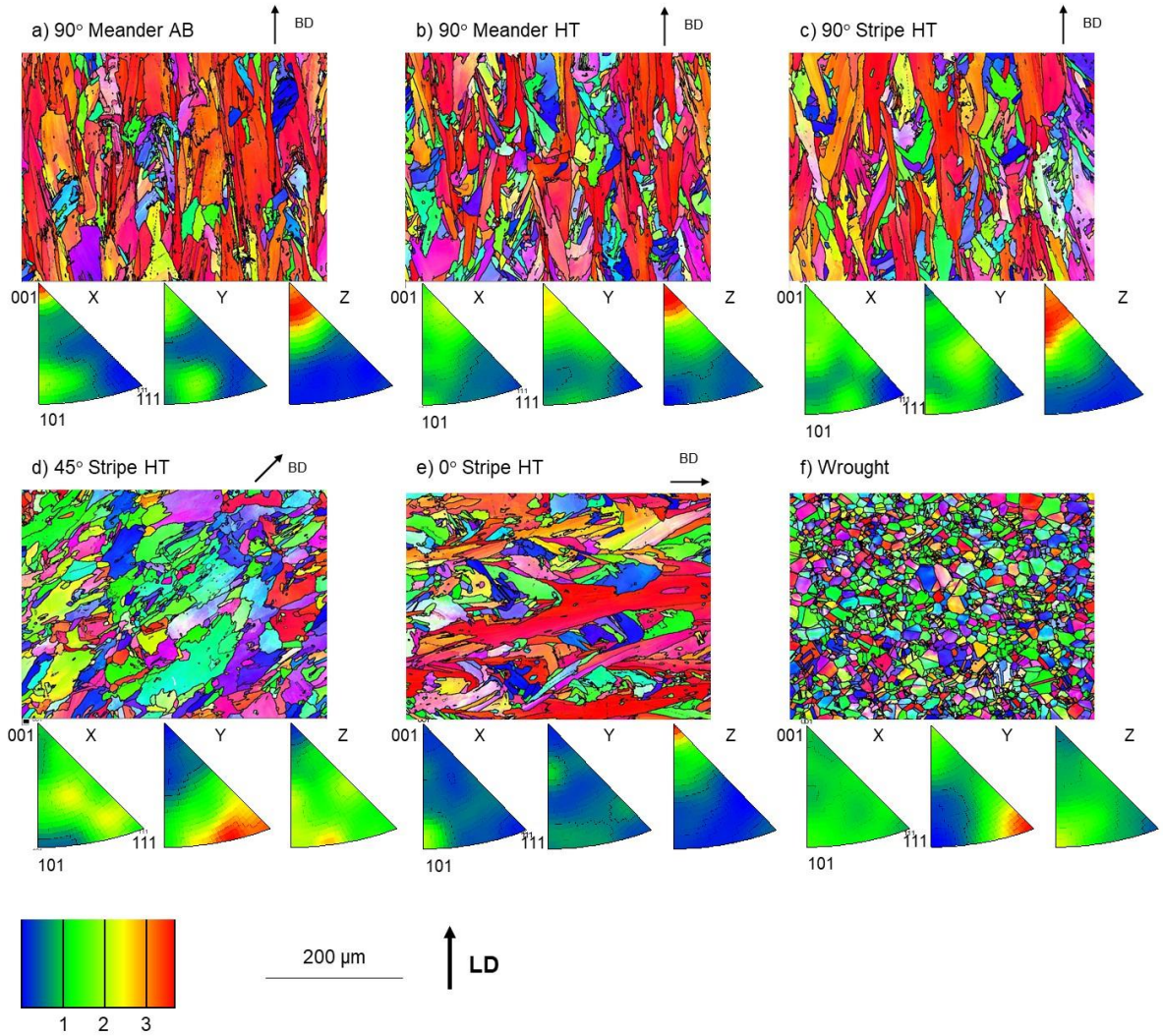

Figure 4: EBSD maps and Inverse Pole Figures for a) 90° Meander AB specimens; Heat treated b) 90° Meander HT; c) 90° Stripe HT; d) 45 ° specimens; e) 0° Stripe HT and f) Wrought alloy 718. All images oriented with respect to the Loading Direction (LD), with the Build Direction (BD) indicated. Most LPBF specimen had a 001 texture parallel to their build direction. It is also clear that heat treatment reduced the texture and that Stripe specimen had a higher texture than their Meander counterpart.

3.2 Creep performance of LPBF specimens

Figure 5 shows a summary of the creep data from all the test cases indicated in Table 2, with 3 repeats for each case. As can be seen, heat treatment, orientation and scan strategy all drastically affect the creep performance. The 90° Meander AB specimens had an inferior creep life, compared to their heat treated counterparts, by a factor of 5, which is in line with other studies [19]. This shows the beneficial effect of heat treatment and confirms the choice to heat treat the remaining specimens. Out of the heat treated specimens, the 90° Meander HT specimen performed 24% better than the wrought specimen in terms of creep life (Figure 6) and overall, specimens built at a 90° orientation to the build plate had a longer creep life than specimens built at 45° and 0°.

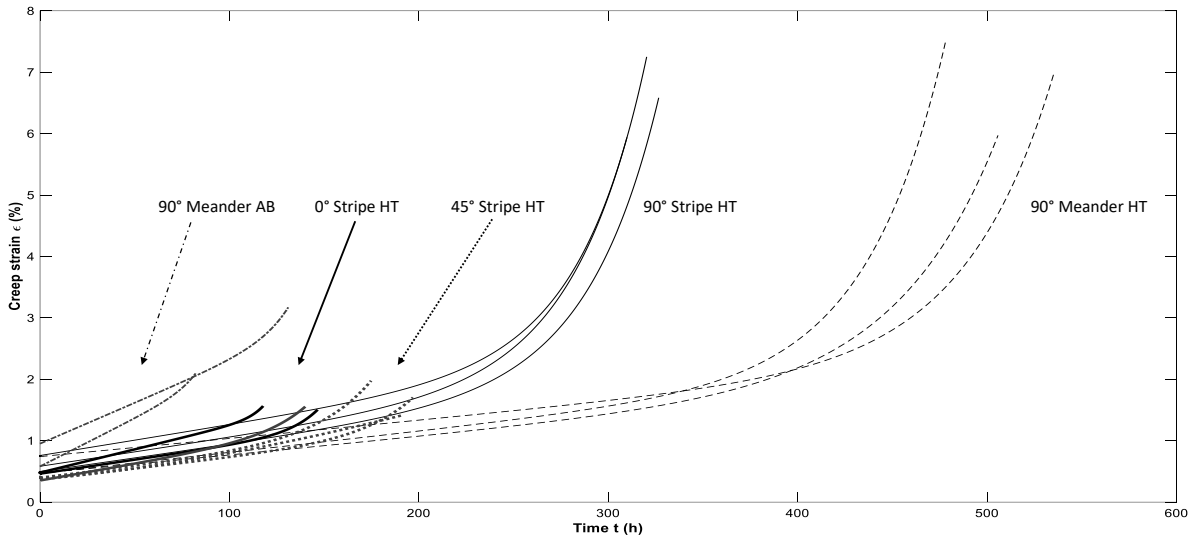

Figure 5: Creep curves for the different test cases, showing the clear differences in creep performance with regards to orientation, heat treatment and scan strategy. This also shows the differences in tertiary creep for the different specimens.

Figure 5 also shows that the creep curves for the various orientation and scan parameters were very different in terms of, secondary creep, tertiary creep and elongation at fracture. Both types of heat treated 90° specimens (i.e. with both Meander and Stripe scan strategies) had a full creep curve with primary, secondary and tertiary creep phases, whereas 0° Stripe HT and 45° Stripe HT specimens failed at the onset of tertiary creep, resulting in an incomplete creep curve and shorter creep life. It is also clear from Figure 6 that the LPBF specimens have a lower elongation at fracture than wrought alloy 718. Indeed, wrought specimens had an elongation at fracture of 29.3%, which in line with literature [33], while 0° Stripe HT specimens had the lowest LPBF elongation of 1.4%. Additionally, Figure 6 shows the creep rates and elongation at fracture of the different specimens and their relation to the creep life. 90° Meander HT specimens had a similar creep rate to the wrought specimen (0.4% difference).

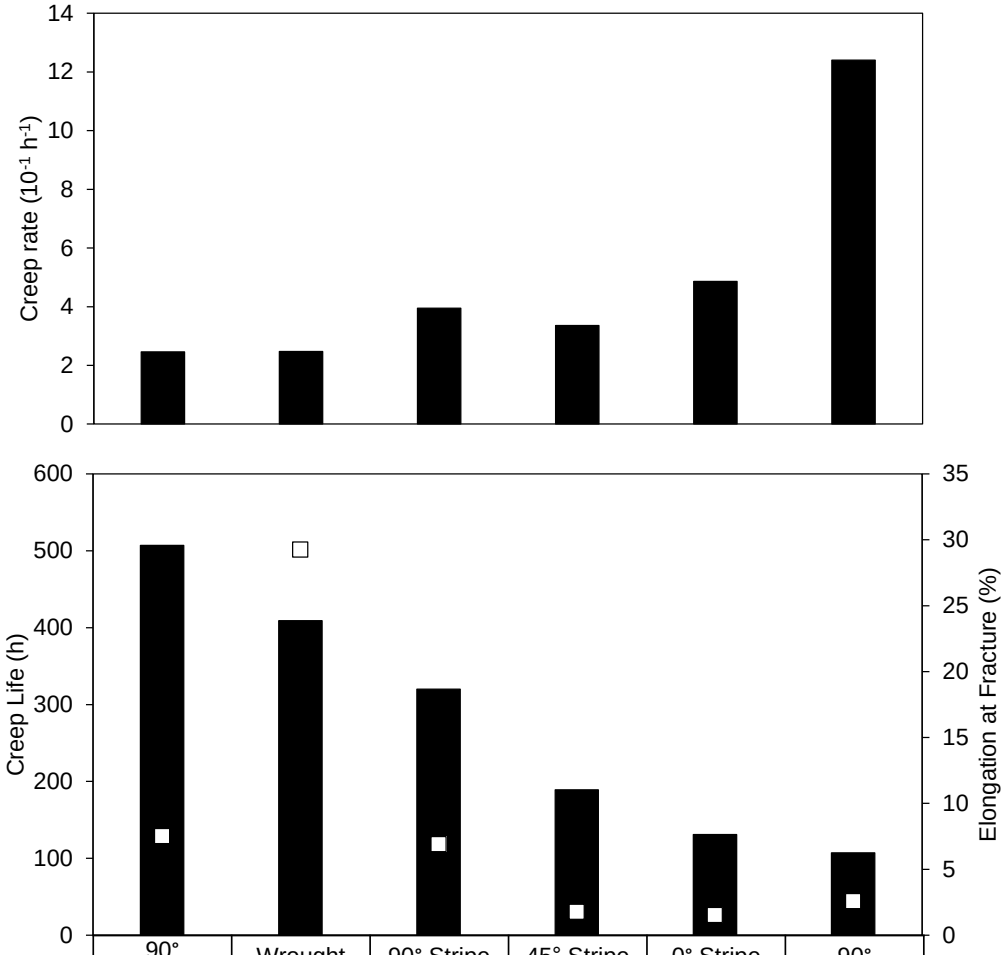

	90° Meander HT	Wrought	90° Stripe HT	45° Stripe HT	0° Stripe HT	90° Meander AB
Creep Life (h)	507 ± 13	409 ± 8	320 ± 4	188 ± 5	131 ± 16	107 ± 17
Creep rate (10^{-1} h^{-1})	2.46 ± 0.1	2.47 ± 0.2	3.95 ± 0.1	3.36 ± 0.2	4.86 ± 0.8	12.4 ± 1.1
Elongation at Fracture (%)	7.5 ± 0.5	29.3 ± 0.1	6.9 ± 0.3	1.8 ± 0.1	1.4 ± 0.1	2.6 ± 0.3

Figure 6: Summary table and graph of the creep rate, elongation at fracture and creep life for all of the test cases, in order of decreasing creep life.

3.3 Fractography of LPBF specimens

This section mainly looks at the differences between microstructural fracture mechanisms and fracture surface indicators to understand how and why specimens failed differently with respect to their different orientations and scan strategies.

3.3.1 Fracture mechanisms

Overall, from a microstructural point of view, a typical creep failure mechanism (i.e. microvoid coalescence) seem to have occurred in all specimens, but to different degrees. All of the specimens had microvoids on the grain boundaries, oriented perpendicular to the loading direction (plane of maximum tensile stress), which shows that creep occurred (Figure 8). Indeed, material separation normal to the loading direction is typical for creep rupture [34] and is a sign of intergranular ductile fracture. The 90° Meander HT and Stripe specimens had the greatest number of coalesced microvoids (Figure 8.b-c). The short side of the grains contained most of those cavities, resulting in V-shaped cracks (Figure 8. b-b' and c-c'). 0° Stripe HT and 45° Stripe HT specimens were similar,

with grain boundaries cavities and δ particles on the long side of the grains (perpendicular to loading direction and parallel to build direction), but in much lower quantity (Figure 8.d-e). 0° Stripe HT specimens also had some transgranular cracks present (Figure 9.b). Hilaire et al. also observed transgranular cracks in tensile testing at 650°C for AB 0° and 90° specimens [29]. This was the case only for heat treated 0° Stripe HT specimens here.

The 45° Stripe HT specimens failed approximately, at a 45° angle with respect to the loading direction, which is a plane of maximum shear stress and the expected plane for ductile failure. The 90° and 0° specimens failed on a plane perpendicular to the loading direction (Figure 8 and Figure 10), which corresponds to the plane of maximum tensile stress. Furthermore, 90° and 45° Stripe HT specimens failed on a plane perpendicular to their build direction while the 0° Stripe HT specimens failed on a plane parallel to their build direction (Figure 7). This shows that where a plane of maximum tensile or shear stress is perpendicular to the build direction, this will be the preferred plane of fracture, as is the case for 90° and 45° specimens. In the case of the 0° specimen, where the plane of maximum tensile stress is parallel to the build direction, the specimen will still fail on the plane of maximum tensile stress. This shows that the stress state of the sample may have a larger impact on the failure mode of the specimen than the build orientation of that specimen. As for Wrought specimens, the failure cross-section presented very few cracks (Figure 8.f) at a low magnification, unlike the 90° specimens. It also had a slight cone and cup outline and necking, signs of a ductile fracture. The biggest defects seemed to be formed around Laves particles (Figure 9.c). At high magnification however, small microvoids were observed in between the δ particles, which is the typical creep mechanism.

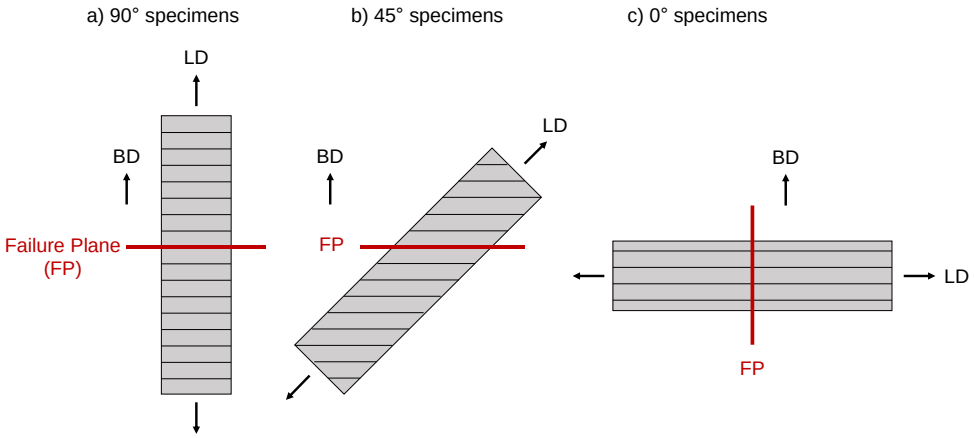

Figure 7: Schematic representation of the failure planes of the different test cases, with respect to specimens' layers, build direction (BD) and with the Loading Direction (LD) shown. This shows that the stress state of the specimen also influenced their modes of failure.

Table 5 quantifies the features observed in the SEM images. Different metrics are used to compare the damage incurred. The crack frequency represents the total area, as a percentage of the total area of the specimen, that incurred cracks. This is a representation of the amount of damage incurred in a specimen. As observed, 90° Stripe HT specimens had the greater number of cracks and amount of creep damage, 89% more than Wrought alloy 718, which had the lowest amount. This is because, as shown in Figure 8.f', microvoids in the wrought material are much smaller than in LPBF specimens. Out of the LPBF specimens, 0° Stripe HT specimens had the lowest amount of damage and cracks, 83% less crack frequency than 90° Stripe HT. Furthermore, the maximum crack length metric gives an idea of how much the microvoids coalesced in the specimens. This could be an indicator of a localised weakness in the material. 0° Stripe HT specimens had the smallest cracks, 96% smaller in length than 90° Stripe HT's largest crack. 0° Stripe HT specimens' damage and cracks were also the closest to the surface. The average distance of cracks from the fracture surface. This measure was obtained by measuring the distance from the fracture surface of the visible cracks in the specimen. A short average distance from the fracture surface shows a localisation of defects and cracks in the specimen, responsible for the location of the failure. This hints to a local weakness in 0° Stripe HT specimens, instead of failure of the material as a whole from creep damage. 90° Meander HT specimens' had cracks the furthest away from the surface due to the even distribution of damage in the part. Therefore, this shows that creep damage has occurred in all of the specimens, despite some creep curves not showing much tertiary creep. The fracture surface will further provide an answer as to what caused failure.

Table 5: Quantification of damage in the different specimens.

Specimen	Crack Frequency (± 0.15 %Area)	Maximum crack length (± 0.5 µm)	Average crack distance from Fracture surface (± 0.01 mm)
90° Meander HT	0.69	674	3.52
90° Stripe HT	**0.82**	**709**	1.48
45° Stripe HT	0.26	317	1.03
0° Stripe HT	0.14	28	**0.19**
90° Meander AB	0.48	260	2.44
Wrought	0.09	175	2.96

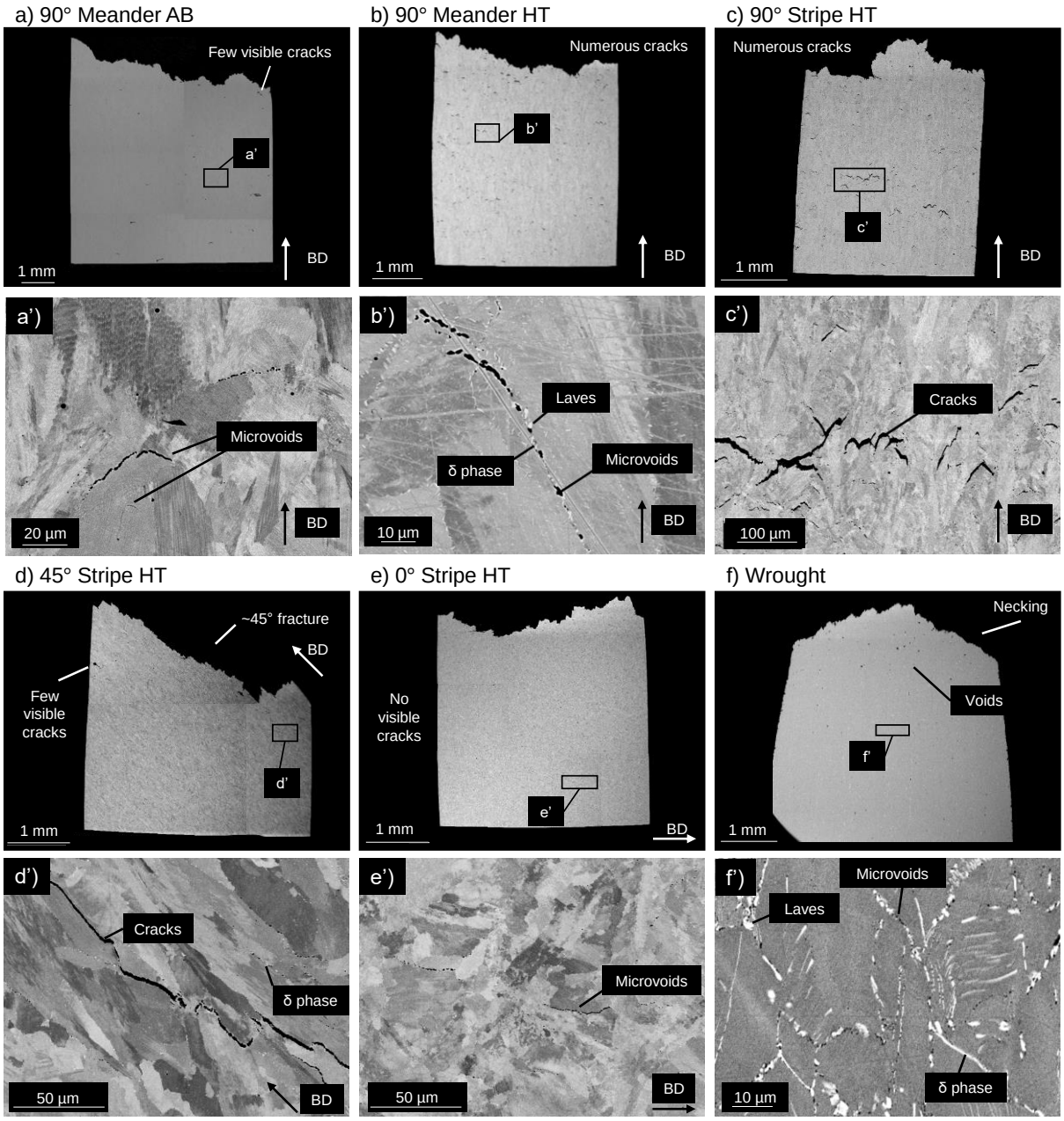

Figure 8: SEM images of the microscopic indicators of the fracture mechanisms for a), a') 90° Meander AB; b), b') 90° Meander HT; c), c') 90° Stripe HT; d), d') 45° Stripe HT; e), e') 0° Stripe HT and f), f') Wrought alloy 718

specimens. All images oriented with respect to the Loading Direction, with the Build Direction (BD) indicated. This shows that microvoids initiated and coalesced along the grain boundaries of the LPBF specimens. In contrast, the wrought sample had very small microvoids, as their coalescence was impeded by the δ precipitates at the grain boundaries.

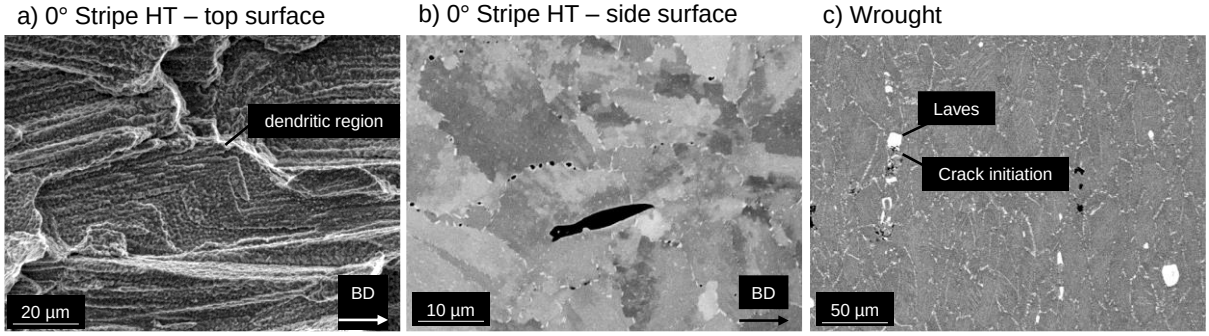

Figure 9: SEM images of a) Trans-dendritic failure surface indicator in 0° Stripe HT specimen; b) Transgranular crack in 0° Stripe HT specimens and c) crack initiation at the Laves phase in Wrought specimens. All images oriented with respect to the loading direction, with the Build Direction (BD) indicated.

3.3.2 Fracture surface

Despite having observed a similar creep mechanism in all specimens, there were significant differences noted in the fracture surfaces with respect to the different orientations and heat treatment. The fracture surfaces of the heat treated 90° specimens presented scan lines from the different scanning strategies (Figure 10.b-c), showing that despite heat treatment, an AM-specific failure still occurred. A similar appearance was noticed after tensile testing at 650℃ for AB 90° and 0° Stripe HT specimens by Hilaire et al. [29]. However, in this work, 0° Stripe HT specimens did not show traces of scanning strategies.

The fracture surfaces of all heat treated 90° specimens showed some signs of a ductile failure with dimples and tear ridges, however, there was no significant necking (Figure 10.a-c). The 0° Stripe HT and 45° Stripe HT specimens also exhibited clear intergranular ductile failure signs, such as dimples and tear ridges, however cleavage steps were also indicating that the specimen actually failed by Quasi-cleavage (Figure 10.d and e). This has been observed in other creep studies [19]. There were also some signs of trans-dendritic failure (Figure 9.a), which was also observed in a high temperature tensile test by Hilaire et al. with AB 0° Stripe specimens where the specimens fractured by shearing [29]. The 45° Stripe HT specimens' fracture surface was at a 30-45° angle and had similar aspects to the 0° Stripe HT surface with few dimples and a rock-candy appearance, which are intergranular failure signs. As this specimen failed at 45° from the loading direction, it may be a sign of failure by mixed mode mechanisms due to the tension from the creep test and the shear stress acting perpendicular to the build direction due to the specimen's grain orientation, which resulted in grain sliding. Wrought specimens had a fibrous appearance with numerous dimples and a shear lip at the specimen edge as well as necking (Figure 10.f). Hence, wrought specimens had a totally ductile failure, as is traditionally the case with nickel-superalloys [35]. 90° Meander AB specimens also had many ductile aspects as well as some cleavage steps (Figure 10.a), similar to the other LPBF specimens. It can be summarised that despite similar microstructural mechanisms, the actual cause of fracture was different for the different test cases.

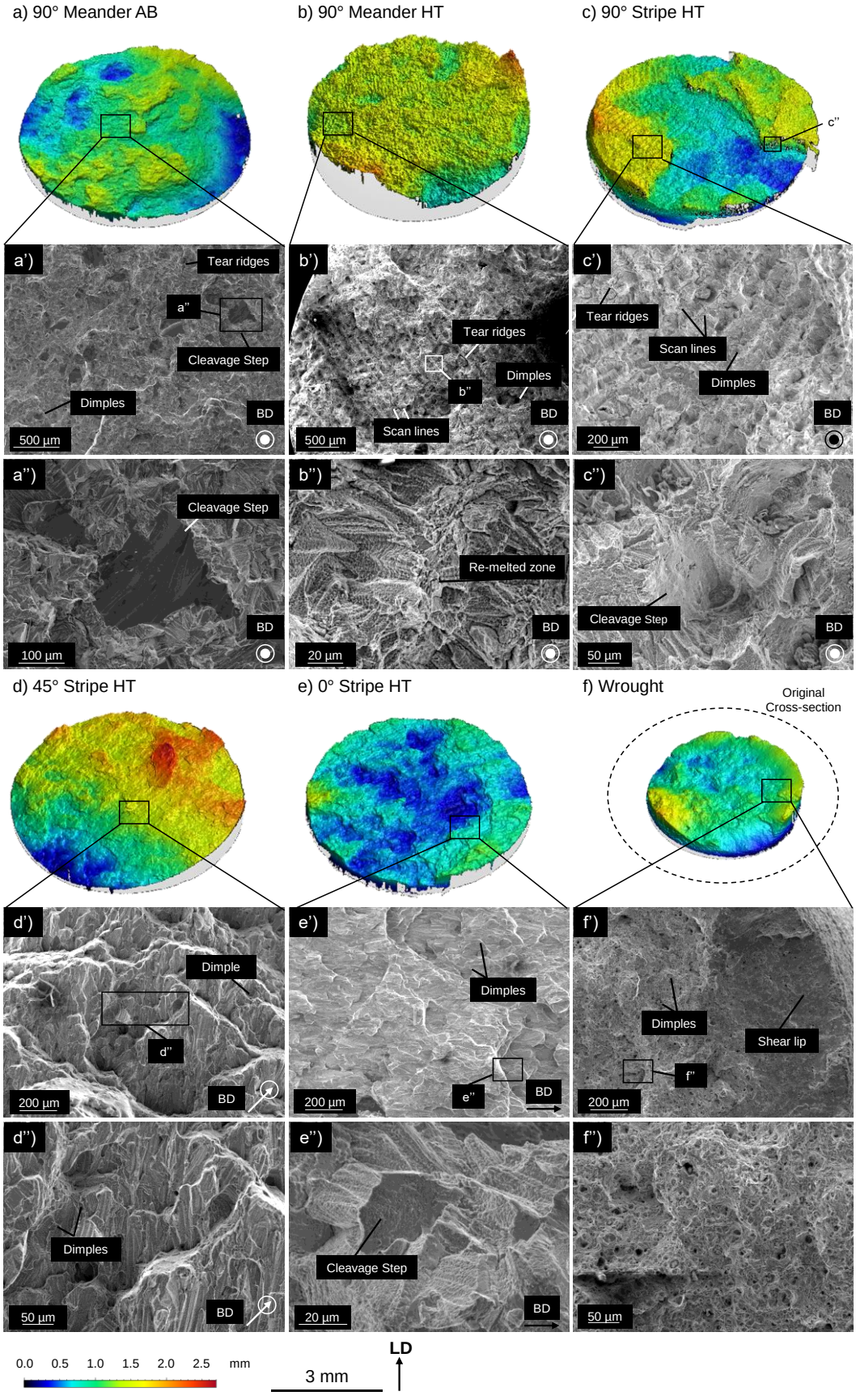

Figure 10: Alicona scans processed by MountainsMaps and SEM images of the fracture surfaces of a) - a'') 90° Meander AB; b) - b'') 90° Meander HT; c) - c'') 90° Stripe HT; d) - d'') 45° Stripe HT; e) - e'') 0° Stripe HT and f) - f'') Wrought alloy 718 specimens. All surfaces showing signs of ductile fracture. All images oriented with respect to the Loading Direction (LD), with the Build Direction (BD) indicated. Most LPBF samples show signs of quasi-

cleavage fracture with dimples and cleavage steps while the Wrought specimen had a fully ductile failure with dimples, a fibrous appearance and shear lip.

4 Discussion

To explain the differences in creep behaviour and failure mode described in the previous section, the effects of microstructural anisotropy and precipitates formation due to heat treatment will be evaluated, followed by a discussion on the effect that LPBF variables, such as build orientation and scanning strategy, have on the subsequent creep behaviour and fracture.

4.1 Effects of Heat Treatment

As stated previously, the 90° Meander AB specimens had a much lower creep life than their heat treated counterparts. This shows the beneficial effect of heat treatment and confirms the choice to heat treat the remaining specimens. This difference in performance for the various test cases can be explained by the microstructural anisotropy and the role of the strengthening precipitates γ'' and δ that appear during heat treatment and impede dislocation motion during creep.

4.1.1 Effect of microstructural anisotropy

The AB specimens' anisotropic microstructure and crystallographic orientation played a role in the poor creep performance. The strong texture in the 001 direction present in AB specimens and absent in its heat treated counterpart, shows that heat treatment reduces some of the in-built LPBF anisotropy and is therefore beneficial to the subsequent creep performance. Indeed, Yu et al. found that the preferred orientations during creep were 001 and 111 [36] and Hsu et al. found that for cadmium, the creep mechanism (grain boundary sliding) was also influenced by texture [37]. This shows that anisotropy and texture can influence the creep properties of materials and may explain the poor performance of some specimens, such as the 45° and 0° Stripe HT. Furthermore, Jiang et al. stated that AB specimens' texture and grain shape resulted in higher hardness and Young's modulus when the loading direction was normal to the build direction, than when build direction and loading direction are parallel [38]. Also, despite having better hardness than the heat treated specimens, the ductility was reduced [38]. Hence, it can be seen that AB LPBF specimens tend to be more brittle than their heat treated equivalents. The low ductility and high hardness of the AB specimens in this study explains the low elongation at fracture and brittle failure at the onset of tertiary creep.

Table 3 showed that the grain size of the various test cases was different despite having similar process parameters and heat treatment. The specimens were heat treated while still being attached to the build plate, which may have acted as a heat source during the cooling down. Indeed, the 45° Stripe HT specimens, which were found to have the largest grains by a factor of 2, were built with numerous supports along its length whilst the 90° specimens (which had the smallest grains of the LPBF specimens) only had the least contact with the build plate and no supports. Having a large contact with this heat source may have slowed the cooling rate and allowed more time for grain growth in the 45° Stripe HT specimens. On another note, although grain size usually increases after heat treatment [39] or Hot Isostatic Pressing [40], the 90° Meander AB specimens were found to have larger grains, by a factor of 1.5, than their heat treated counterparts (Table 3). This observation is explained by the very long and elongated columnar grains in the AB sample, which although have small diameters, represent a larger grain area than the slightly bigger diameter grains in the 90° Meander HT specimen. Another reason for the smaller grain area of 90° Meander HT specimens is that while the heat treatment partially-recrystallised the grains and resulted in more defined grain boundaries, it did not necessarily increase grain size. Zhao et al. also showed that grain size in LPBF alloy 718 did not vary significantly after a solution treatment at 1080°C [41] and hence, due to the different starting microstructures between LPBF and conventional nickel alloys, the heat treatment is not optimised and does not yet result in larger and fully recrystallised grains in LPBF specimens. This shows that further work on heat treatment optimisation for LPBF alloy 718 could result in better control of the mechanical properties of the material.

It is well known that larger grains are beneficial for creep performance [42]. The differences in grain size for the different test cases showed that, for the LPBF specimens, an increasing grain size was detrimental to both creep rupture time and creep strain rate until a certain point (above ~200 μm^2 here) after which an increasing grain size started to be beneficial (Figure 11). The wrought specimens had significantly smaller grains, by at least 57%, than any of the LPBF specimen (Figure 11) while its creep life and creep rate outperformed the majority of LPBF

specimens. Previous studies on the creep of wrought alloy 718 found that an increasing grain size reduced the total creep rupture time [34] whereas Xu et al. found that forged specimen performed better than their LPBF counterparts due to their small equiaxed grains [43]. Indeed, Xu et al. stated that the large columnar grains present in LPBF specimens have difficulty rotating locally during the creep deformation process, unlike the small equiaxed grains of the forged material which are able to rotate and reduce the stress concentration at the grain boundaries, hindering crack initiation and propagation [43].

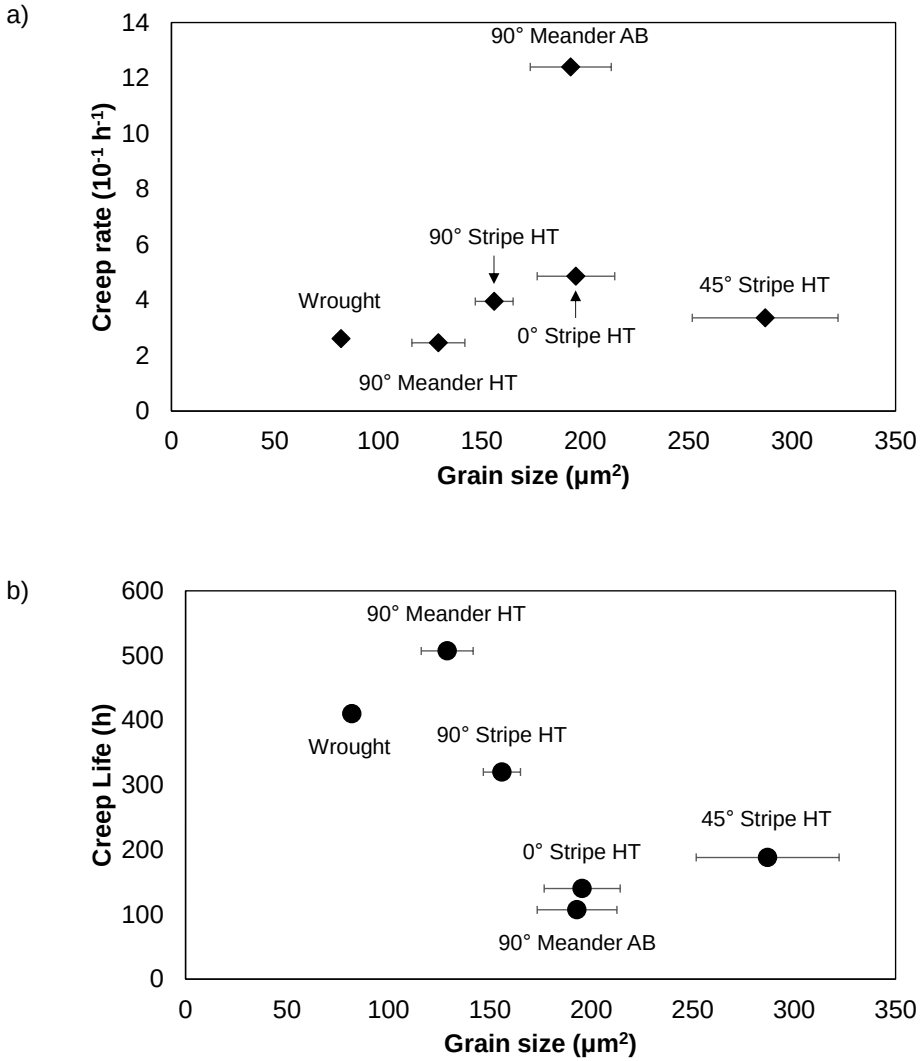

Figure 11: Relationship between the grain size and a) the creep rate and b) the creep life for the different test cases.

4.1.2 Effect of precipitates

Chen et al. investigated a number of precipitate-enhancing heat treatments in order to optimise precipitate density in wrought alloy 718 [34]. Precipitate density ranged from 0-70 % in the study mentioned and it was shown that having a precipitate density higher than 45% resulted in longer creep rupture time [34]. The γ'' phase is the main strengthening phase of alloy 718 for creep performance and is closely linked to the δ-phase as in 650°C to 980°C range, γ" transforms into the detrimental δ-phase. It is therefore clear that precipitates play a role in the creep performance of materials. Although the γ'' phase is known to be the main strengthening phase, this discussion will focus on the effects of the δ-phase and Laves phase and how these detrimental phases could potentially be controlled and improve creep performance through optimised heat treatment.

Wrought specimens had the highest density of δ precipitates in this study, 7 times more than the LPBF specimen with the highest precipitate density (0° Stripe HT) and AB Meander HT had no precipitates, although Laves phases were present (Figure 3.a). This is because precipitates emerge from heat treatment and hence, one of the possible

reasons why the wrought specimens had a higher percentage of precipitates is that the heat treatment standard used was developed with a wrought microstructure in mind as a starting point. The fact that LPBF materials have an anisotropic microstructure of elongated columnar grains and equiaxed grains in different directions, dissimilar to wrought or cast materials which have an almost isotropic microstructure, means that the heat treatment is not optimal as it was not designed specifically for this starting microstructure. Huang et al. researched new heat treatments for LPBF alloy 718 and found that a reducing the cooling rate contributed to the precipitation of strengthening precipitates and that a lower solution time is required, compared to alloy 718 ingots [44]. Furthermore, they found that LPBF materials have a faster ageing response compared to wrought material which led to the dissolution of Laves phases and allowed a higher precipitation of strengthening phases, resulting higher tensile strength and ductility [44]. However, Huang et al. mainly studied the result of different heat treatments on tensile properties and hence, more research is needed following their work to obtain a heat treatment that would increase LPBF alloy 718 creep properties.

Figure 3 shows that the δ precipitates in wrought specimens had a significant size range (particles size ranged from 1 μm to 12 μm) compared to the 90° Meander HT specimens which had the lowest density of δ-precipitates and had δ ranging about 0.5 μm to 1 μm. Although, δ precipitates were stated to serve as void initiation points [34, 43] this present study argues that the size and number of those particles was an impediment to microvoid formation and coalescence. Indeed, the size of the δ particles on the grain boundaries in the wrought specimen meant that there was very little space for microvoids to form and link (Figure 8.f), hence impeding microvoid coalescence and slowing down the creep rate. Xu et al. also observed that in heat treated samples of LPBF alloy 718, δ-phase hindered crack growth and improved creep performance [19]. Chen et al. suggested that for wrought alloy 718 low densities of δ precipitates would isolate creep voids, resulting in fracture mainly due to wedge cracks at triple point grain boundaries, whereas a high density of precipitates would mean that the fracture would be controlled by cavity growth and grain boundary sliding [34]. Although the precipitate density was low in LPBF specimens, it seems that the latter was the cause of fracture. Additionally, Yeh et al. found that the precipitation of δ particles during the heat treatment of wrought alloy 718 influenced the morphology of grain boundaries, which in turn resulted in an extended creep life [45]. Xiao et al. also reported that they could control the precipitation of δ and γ'' precipitates in alloy 718 by using a Quasi–Continuous wave laser at different frequencies [46]. This shows that the quantity and size of δ particles and Laves phase have an effect on the creep behaviour of materials. Furthermore, there is potential for improvement in creep performance by modifying the amount of δ-precipitates through heat treatment and LPBF parameters. However, despite having significantly more δ-precipitates, wrought specimens still had a lower creep life and a similar creep rate to the 90° Meander HT specimens. This means that other factors, such as the presence of Laves, grain size, porosity etc must also be affecting the creep behaviour. This will be discussed next.

As well as precipitating strengthening phases, heat treatment is also used to dissolve detrimental phases such as the Laves phase. Since AB was not heat treated, Laves phase was present and may have contributed to the lack of ductility observed, as shown by Schirra et al. [47]. However, their size was much smaller than the Laves phase present in the wrought specimens, due to the high solidification rate during LPBF [44]. As well as the Laves phase, Aydinöz et al. found that the sub-micron cell structures and ill-defined grain boundaries (Figure 3 a-a'') of AB specimens resulted in their lack of ductility [48]. Gribbin et al. also found that the ductility and rupture life of direct laser melted alloy 718 during low cycle fatigue were lower, compared to wrought and cast equivalents, mainly because of the presence of porosity caused by the AM process [49]. Therefore, the main reasons why LPBF materials, heat treated or not, had lower elongation at fracture and hence, lower ductility than wrought alloy 718 was due to the presence of Laves phases and process-related defects such as porosity. With a more optimal thermal treatment, the lack of ductility could be reduced, as was shown by Aydinöz et al. who demonstrated that Hot Isostatic Pressing resulted in an increase in ductility [48].

The Laves phase was detrimental to creep performance as, in line with other studies, Laves phase has been found to serve as crack initiation points [50]. Within this study, this was most evident in Figure 9.c where the largest cracks in the wrought material were formed around Laves phase. Hence, despite the fact that not all Laves phases were dissolved in heat treated specimens, the lesser quantity proved beneficial to creep performance. However, recent studies by Sui et al. found that the morphology and distribution of Laves phases can be beneficial to mechanical properties [51, 52]. Creep was not one of the properties addressed in Sui et al.'s study and hence, future work could involve determining if Laves phases can prove beneficial to creep properties and hence, a specific heat treatment could be designed to optimise, not only grain size but also the precipitation of the different alloy 718 phases to obtain optimal creep performance. Indeed, although heat treatment greatly improved creep

performance, it is still not optimal as the failure mechanisms were mostly AM specific (scan lines, grain orientation and texture). Grains were not fully recrystallized, δ precipitate densities were low and the Laves phase was not fully dissolved. Huang et al. states that when the solution temperature is below 1130°C (which was the case for the present study), the original dendritic microstructure is replaced by partially recrystallised grains that retain their orientation and that Laves phases are not fully dissolved [44]. The ideal heat treatment for LPBF alloy 718, according to Huang et al., is: 1080°C/45 min, AC +700°C/12h +620°C/6h, AC [44]. However, this was not specifically shown to have good results for creep properties and hence, some future attention should be given to the optimisation of heat treatment for subsequent creep performance improvement.

4.2 LPBF build parameter effects on Creep behaviour

The differences in creep rate, creep life and failure for the different specimens can be attributed to the effects of build orientation and scan strategy, which in turn affect the microstructure. These relationships are discussed in more detail in this section.

4.2.1 Effects of build orientation

Figure 5 and Figure 10 showed that specimen fracture was dependant on the building direction. On average, the 90° Stripe HT specimens had a 144% and 70% longer creep life than the 0° Stripe HT and 45° Stripe HT specimens (Figure 6), respectively, which is in line with findings from the literature [53]. However, this is the opposite of the trend observed in other mechanical tests, such as tensile tests, where the 0° Stripe HT specimen performed better than the 90° ones [29].

Furthermore, there was no clear difference in failure surface and mechanism between the 90° Stripe HT and 90° Meander HT specimens (save the different scan tracks), which shows that the failure mechanism is dominated by specimen orientation and by continuation, the grain orientation (Figure 10). As stated previously, the 45° Stripe HT and 90° specimens failed on a plane perpendicular their build direction (on a layer) while 0° Stripe HT specimens failed on a plane parallel to the build direction. This shows that the build direction of the specimens plays a significant part in the resulting failure mode. For the 45° Stripe HT specimens, because of the particular orientation of the grain boundaries, it seems that the failure was due to mixed mode loading I and II. Indeed, although a fracture on a plane at a 45° angle is usually a sign of ductile failure, the orientation of the grains with respect to the loading direction provided an opportunity for grain boundaries sliding which induced a premature mixed mode fracture. Hovig et al. observed a similar phenomenon with the fracture of a 45° Stripe HT tensile specimen where the grain boundaries aligned with the slip line and caused decohesion [54]. They also noticed that when grains were parallel to the loading direction, this limited the possibility of a pure Mode I failure [54]. Although it is possible that creep damage is present in a different plane with respect to the loading direction, the implication is that the 45° Stripe HT specimens did not fail because of creep damage but due to their oriented LPBF microstructure. Furthermore, the 0° Stripe HT specimens had few cracks (Table 5), which were all located close to the fracture surface on the side of grains oriented perpendicularly to the loading direction. The orientation of the grains facilitated Mode I tensile opening and the initiation and coalescence of microvoids, leading to faster creep rate and lower elongation at fracture than 90° Stripe HT specimens. This is in line with tensile test of LPBF alloy 718 findings from Ni et al. which found accelerated damage in horizontal specimen, as compared to vertical ones, leading to lower elongation but higher tensile strength [55]. McLouth et al. also found that elongated grains parallel to the loading direction (i.e. in similar conditions than the 90° specimens in the present work) increased the time to rupture and the ductility of LPBF 718 samples [13]. Figure 12 shows the schematic crack path for the different specimens due to their grain orientation. This figure shows that the 90° and the 45° specimens failed preferentially between layers while the 0° specimens failed between melt pools. This is probably due to the stresses acting on the samples, which causes the 90° and the 0° specimen to fail on the plane of maximum tensile stress. Interestingly, the 45° specimens failed on the plane of maximum shear stress which is likely caused by their microstructure and the fact that damage accumulated on the grain boundaries which are aligned with that plane. It would be beneficial to test more building angles in order to determine the cause and the point where specimens stop failing from between layers to between meltpools.

The crystallographic texture may also be partly responsible for the different creep performance for the different build orientations as there is mostly a higher texture in the build direction of specimens (Figure 4). Indeed, Ni et al. suggested that the differences in ductility and strength in LPBF samples was in part caused by the {100} fibre texture in samples which was thought to result in higher strength perpendicular to the build direction [55]. This

higher strength perpendicular to the build direction likely proved beneficial to the 90° specimens as this strengthened their failure plane, but may be one of the reasons why 0° Stripe HT specimen performed more poorly.

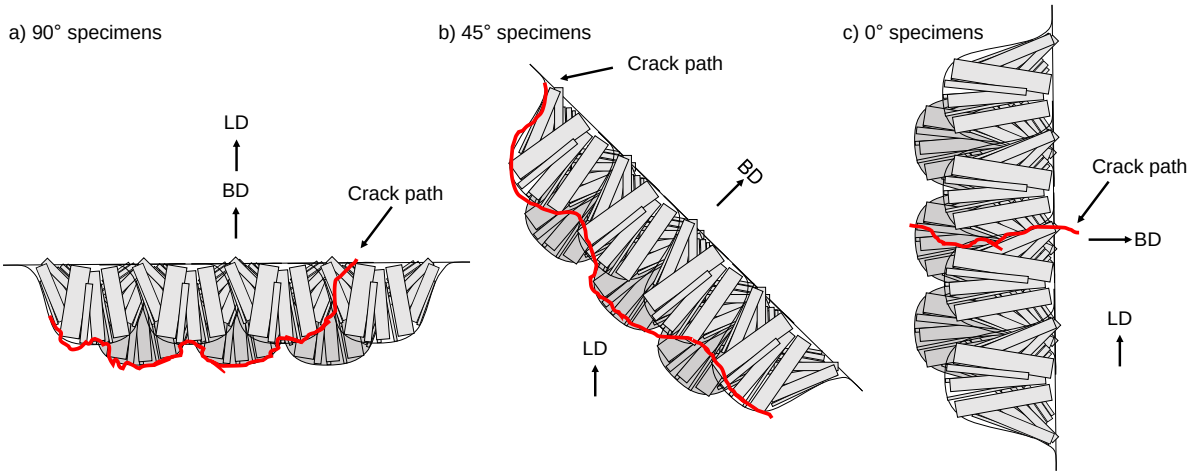

Figure 12: Crack path for a) 90° specimens, where intergranular cracking occurred with some cleavage steps; b) 45° Stripe HT specimens where the intergranular cracking caused grain boundaries decohesion and sliding; and c) 0° Stripe HT specimens where Quasi-Cleavage occurred. All images oriented with respect to the Loading Direction (LD), with the Build Direction (BD) indicated.

Other than the effects of grains and texture orientation, the orientation of δ precipitates may also have an effect on the creep rupture life. Due to of the build orientation, LPBF specimens had elongated grains in the build direction. This means that the majority of grain boundaries and hence, of δ precipitates, were in line with the build direction. Hence, for the 90° specimens, the precipitates were aligned with the loading direction while they were normal to the loading direction for 0° Stripe HT specimens. Indeed, the orientation of the δ precipitates, normal to the loading direction for the 0° Stripe HT specimens is likely the reason for the reduced creep life, as also shown by Kuo et al. [53] and may explain the lack of observed tertiary creep. Although δ precipitates have a relatively small lattice mismatch, there is still a mismatch and hence, it could be a point of weakness in the specimen that causes an early fast fracture instead of a creep fracture. This mismatch could also be a contributing factor in the grain sliding seen in the 45° Stripe HT specimen. This shows that the spatial orientation of defects and dendrites are important features in the damage evolution process [29]. What's more, it is also clear from Figure 3 and Table 3 that the differences in precipitate density for the different test cases is not caused by build orientation in the LPBF specimens. Indeed, the 90° Meander HT and 90° Stripe HT have 43% difference in precipitate densities whilst the 45° Stripe HT and 0° Stripe HT specimens have a similar amount. Hence, it is possible that the scan strategy was responsible for the difference in precipitate density.

4.2.2 Effects of the Scanning Strategy

The 90° Meander HT and 90° Stripe HT specimens have a 58 % difference in creep rupture time, a 38% difference in creep rate, a 17% difference in grain size and a 43% difference in precipitate density, whereas only the scan strategy is different. The differences between 90° Stripe HT and 90° Meander HT may be explained by the lesser quantity of laser overlapping zones in the 90° Meander HT specimen. The laser overlapping areas undergo some re-melting that results in larger grains parallel to the build direction, due to the slower cooling rate caused by the 2nd heat input. This 2nd heat input causes the columnar grains to rotate [56], resulting in equiaxed grains normal to the build direction. This equiaxed overlapping laser region was also observed here (Figure 3) and by Ahmad et al. [57] and Choi et al. also states that the laser overlapping area is subject to complex heat flows which changes the orientation of the grains and results in equiaxed microstructure at the melt-pool boundaries [58]. This was also observed in modelling of the microstructure of LPBF 316L Stainless Steel [59]. The columnar grains were stated to grow from the boundary towards the centre of the melt-pool while equiaxed grains were formed by supercooling at the boundaries [60]. Parimi et al. also observed inter-layer equiaxed grain structure [61]. These equiaxed areas can be observed in the planes normal to the build direction in Figure 3 and a schematic representation is shown in Figure 13. These small equiaxed grains provided more grain boundaries, which may have been detrimental to the creep properties. Indeed, since cavities form on grain boundaries and that laser overlapping areas results in more

numerous grain boundaries, this may have been the cause of the faster creep rate and shorter creep life of 90° Stripe HT specimens as compared to Meander specimens. Furthermore, other studies have shown that there is an increase in porosity at the end of a scan track [62] and that the higher heat input present in the laser overlapping regions causes more porosity and defects [63]. Hence, the bigger stripe offset of -0.4 mm in the 0° Stripe HT specimens probably resulted in defects which could be acting as crack initiation points and favour crack propagation in this region, affecting its creep behaviour. The fact that 90° Stripe HT specimens have more laser overlap regions may mean that there is an increased chance that defects and porosities are present and affecting the creep rate.

The higher quantity of laser overlapping zones in the Stripe strategy could also be responsible for the higher density of δ-particles (Table 3). Indeed, the equiaxed grains mean that there is a higher density of grain boundaries and hence, a higher density of δ precipitates in Stripe specimens. The laser overlap areas could have less creep resistance due to the small grains and the higher concentration of δ particles perpendicular to the loading direction. If so, this would explain the presence of scan tracks on the fracture surface. Indeed, the laser overlapping areas could have provided an "easier" crack propagation area than the rest of the meltpool and grain boundaries. This means that crack tended to preferentially propagate around the grain boundaries and meltpools until reaching a laser overlap zone (as shown in Figure 12.a). Hence, when material separation occurred, the crack path followed the scanning strategy employed (Figure 8 b-b'' and c-c'').

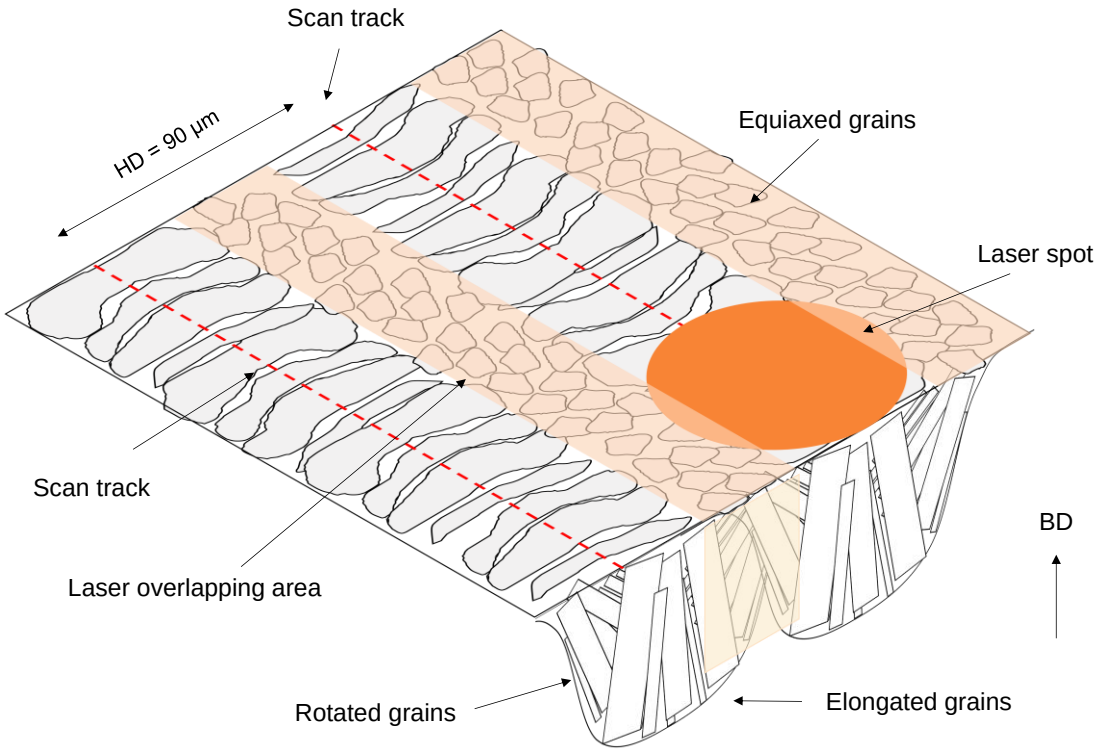

Figure 13: Meltpool and grain formation schematic, showing the columnar and equiaxed grains. With the Build Direction (BD) and Hatch Distance (HD) indicated.

5 Conclusions

To conclude, this paper investigated the effects of LPBF build orientation, scanning strategy and heat treatment on the creep performance of alloy 718. The results showed that the best creep performance was obtained for 90° specimens with a Meander scanning strategy which obtained a creep life 24% longer than the wrought alloy 718 specimen and a similar creep rate to the latter. The key findings can be summarised as:

- Heat treatment reduces anisotropy and improves creep life by partial recrystallization of the grains, dissolution of Laves phase, precipitation of δ-phase and by reducing the crystallographic texture.

- The density, size and orientation of δ precipitates is key for creep performance as they impede void coalescence and hence slow the creep rate.
- The build orientation and stress state of the specimen are responsible for the different failure modes, which all had ductile indicators with some cleavage steps. The various test cases presented different degrees of creep damage (microvoid coalescence).
- The scanning strategy is responsible for the quantity of laser overlapping regions which have poorer creep resistant due to the presence of small equiaxed grains and a higher density of δ particles. Perpendicular to the loading direction, these particles can increase the brittleness of the specimen and result in a lower creep resistance.
- Further research should be done on:
  - Heat treatments as those investigated to date are not LPBF specific and hence result in sub-optimal precipitation, poor Laves dissolution and partial grain recrystallisation.
  - The effect of orientation on the creep failure mechanism.
  - Developing an optimum scanning strategy with as little laser overlapping zones as possible.

Overall, this paper provides an insight into LPBF specific effects on the creep performance of nickel superalloys.

Acknowledgments

This work has been supported by the Engineering and Physical Sciences Research Council [EP/S513854/1]. Thank you to Shane Maskill for his creep testing expertise and for grinding the specimens, Alex Jackson-Crisp for machining specimens, Nigel Neate and the University of Nottingham nano and microscale Research Centre for additional SEM and EBSD imaging, James Murray for conducting the Alicona scans and Alistair Speidel for assisting with the use of MountainsMaps and ImageJ software.

Data Availability

The raw/processed data required to reproduce these findings cannot be shared at this time due to technical or time limitations.

References

1. Chua, C.K., *3D printing and additive manufacturing : principles and applications (the 5th edition of Rapid prototyping : principles and applications)*. 5th ed. / Chee Kai Chua, Kah Fai Leong. ed. Three dimensional printing and additive manufacturing, ed. K.F. Leong. 2017, Singapore: Singapore : World Scientific.
2. Ashby, M.F., *Engineering materials 1 : an introduction to properties, applications and design / by Michael F. Ashby, David R.H. Jones*. 4th ed. ed. Engineering materials one, ed. D.R.H. Jones. 2012, Oxford: Butterworth-Heinemann.
3. Geddes, B., H. Leon, and X. Huang, *Superalloys : alloying and performance*. 2010, Materials Park, OH: ASM International.
4. Carter, L.N., *Selective Laser Melting of nickel superalloys for high temperature applications*, in *School of Metallurgy and Materials*. 2013, University of Birmigham: Birmigham.
5. Chlebus, E., K. Gruber, B. Kuźnicka, J. Kurzac, and T. Kurzynowski, *Effect of heat treatment on the microstructure and mechanical properties of Inconel 718 processed by selective laser melting.* Materials Science and Engineering: A, 2015. **639**: p. 647-655.
6. Schirra, J.J., R.H. Caless, and R.W. Hatala, *The Effect of Laves Phase on the Mechanical Properties of Wrought and Cast + HIP Inconel 718*. 1991. 375-388.
7. Konečná, R., L. Kunz, G. Nicoletto, and A. Bača, *Long fatigue crack growth in Inconel 718 produced by selective laser melting.* International Journal of Fatigue, 2016. **92**(Part 2): p. 499-506.
8. Song, H., T. McGaughy, A. Sadek, and W. Zhang, *Effect of structural support on microstructure of nickel base superalloy fabricated by laser-powder bed fusion additive manufacturing.* Additive Manufacturing, 2019. **26**: p. 30-40.
9. Xu, Z., C.J. Hyde, A. Thompson, R.K. Leach, I. Maskery, C. Tuck, and A.T. Clare, *Staged thermomechanical testing of nickel superalloys produced by selective laser melting.* Materials & Design, 2017. **133**: p. 520-527.

10. Roehling, T.T., S.S.Q. Wu, S.A. Khairallah, J.D. Roehling, S.S. Soezeri, M.F. Crumb, and M.J. Matthews, *Modulating laser intensity profile ellipticity for microstructural control during metal additive manufacturing.* Acta Materialia, 2017. **128**: p. 197-206.
11. Simonelli, M., Y. Tse, and C. Tuck, *Effect of the build orientation on the mechanical properties and fracture modes of SLM Ti-6A1-4V.* Materials Science and Engineering: A, 2014. **616**: p. 1–11.
12. Hautfenne, C., S. Nardone, and E. De Bruycker, *Influence of heat treatments and build orientation on the creep strength of additive manufactured IN718*, in *4th International ECCC Conference*. 2017: Düsseldorf Germany.
13. McLouth, T.D., D.B. Witkin, G.E. Bean, S.D. Sitzman, P.M. Adams, J.R. Lohser, J.-M. Yang, and R.J. Zaldivar, *Variations in ambient and elevated temperature mechanical behavior of IN718 manufactured by selective laser melting via process parameter control.* Materials Science and Engineering: A, 2020. **780**: p. 139184.
14. Azarbarmas, M., M. Aghaie-Khafri, J.M. Cabrera, and J. Calvo, *Dynamic recrystallization mechanisms and twining evolution during hot deformation of Inconel 718.* Materials Science & Engineering A, 2016. **678**(C): p. 137-152.
15. *Nickel Alloy, Corrosion and Heat Resistant, Bars, Forgings, and Rings, 52.5Ni - 19Cr - 3.0Mo - 5.1Cb - 0.90Ti - 0.50Al - 18Fe, Consumable Electrode or Vacuum Induction Melted, 1950 °F (1066 °C) Solution Heat Treated, Precipitation Hardenable*. 1965, SAE International.
16. Lambert, D.M., *IN718 additive manufacting properties and influences*, in *JANNAF Conference*, R.E. Group, Editor. 2015: Nashville, TN.
17. Yadollahi, A., M.J. Mahtabi, A. Khalili, H.R. Doude, and J.C. Newman, *Fatigue life prediction of additively manufactured material: Effects of surface roughness, defect size, and shape.* Fatigue & Fracture of Engineering Materials & Structures, 2018. **41**(7): p. 1602-1614.
18. Popovich, V.A., E.V. Borisov, V. Heurtebise, T. Riemslag, A.A. Popovich, and V.S. Sufiiarov, *Creep and Thermomechanical Fatigue of Functionally Graded Inconel 718 Produced by Additive Manufacturing.* 2018: p. 85-97.
19. Xu, Z., C.J. Hyde, C. Tuck, and A.T. Clare, *Creep behaviour of inconel 718 processed by laser powder bed fusion.* Journal of Materials Processing Technology, 2018. **256**.
20. ASTM International, *Standard Test Methods for Tension Testing of Metallic Materials*. 2016, ASTM International: West Conshohocken, PA.
21. Aerospace Material Specification, *Nickel Alloy, Corrosion and Heat Resistant, Bars, Forgings, and Rings 52.5Ni 19Cr 3.0Mo 5.1Cb 0.90Ti 0.50Al 18Fe, Consumable Electrode or Vacuum Induction Melted 1775°F (968°C) Solution Heat Treated, Precipitation Hardenable*. 1965, SAE International.
22. Guo, Q., C. Zhao, L.I. Escano, Z. Young, L. Xiong, K. Fezzaa, W. Everhart, B. Brown, T. Sun, and L. Chen, *Transient dynamics of powder spattering in laser powder bed fusion additive manufacturing process revealed by in-situ high-speed high-energy x-ray imaging.* Acta Materialia, 2018. **151**: p. 169-180.
23. ASTM International, *Standard Test Methods for Conducting Creep, Creep-Rupture, and Stress-Rupture Tests of Metallic Materials*. 2018, ASTM International: West Conshohocken, PA.
24. Buehler. *SumMet method for Ni-based Superallys*. 2020 [cited 2020 05/2020]; Available from: https://www.buehler.co.uk/sumMet.php?material=Ni%20%26%2345%3BBased%20Superallys.
25. Li, X., J.J. Shi, C.H. Wang, G.H. Cao, A.M. Russell, Z.J. Zhou, C.P. Li, and G.F. Chen, *Effect of heat treatment on microstructure evolution of Inconel 718 alloy fabricated by selective laser melting.* Journal of Alloys and Compounds, 2018. **764**: p. 639-649.
26. Wu, X., J. Liang, J. Mei, C. Mitchell, P.S. Goodwin, and W. Voice, *Microstructures of laser-deposited Ti–6Al–4V.* Materials & Design, 2004. **25**(2): p. 137-144.
27. Sabelkin, V.P., G.R. Cobb, T.E. Shelton, M.N. Hartsfield, D.J. Newell, R.P. O'Hara, and R.A. Kemnitz, *Mitigation of anisotropic fatigue in nickel alloy 718 manufactured via selective laser melting.* Materials & Design, 2019. **182**: p. 108095.
28. Cao, Y., P. Bai, F. Liu, and X. Hou, *Investigation on the precipitates of IN718 alloy fabricated by selective laser melting.* Metals, 2019. **9**(10).
29. Hilaire, A., E. Andrieu, and X. Wu, *High-temperature mechanical properties of alloy 718 produced by laser powder bed fusion with different processing parameters.* Additive Manufacturing, 2019. **26**: p. 147-160.
30. Pham, M.-S., B. Dovgyy, P.A. Hooper, C.M. Gourlay, and A. Piglione, *The role of side-branching in microstructure development in laser powder-bed fusion.* Nature Communications, 2020. **11**(1): p. 749.

31. Newell, D.J., R.P. O'Hara, G.R. Cobb, A.N. Palazotto, M.M. Kirka, L.W. Burggraf, and J.A. Hess, *Mitigation of scan strategy effects and material anisotropy through supersolvus annealing in LPBF IN718.* Materials Science and Engineering: A, 2019. **764**: p. 138230.
32. Thijs, L., M.L. Montero Sistiaga, R. Wauthle, Q. Xie, J.-P. Kruth, and J. Van Humbeeck, *Strong morphological and crystallographic texture and resulting yield strength anisotropy in selective laser melted tantalum.* Acta Materialia, 2013. **61**(12): p. 4657-4668.
33. Hayes, R.W., *Creep Deformation of Inconel alloy 718 in the 650°C to 760°C temperature regime*, in *Superalloys 718, 625 and Various Derivatives*, E.A. Lorin, Editor. 1991: Northridge, California.
34. Chen, W. and M.C. Chaturvedi, *Dependence of creep fracture of Inconel 718 on grain boundary precipitates.* Acta Materialia, 1997. **45**(7): p. 2735-2746.
35. Cui, L., H. Su, J. Yu, J. Liu, T. Jin, and X. Sun, *The creep deformation and fracture behaviors of nickel-base superalloy M951G at 900 °C.* Materials Science and Engineering: A, 2017. **707**.
36. Yu, Z., H. Jing, L. Xu, L. Zhao, and Y. Han, *Microstructure and texture study on an advanced heat-resistant alloy during creep*. Materials Characterization, 2017. **130**.
37. Hsu, S.-e., G.R. Edwards, and O.D. Sherby, *Influence of texture on dislocation creep and grain boundary sliding in fine-grained cadmium.* Acta Metallurgica, 1983. **31**(5): p. 763-772.
38. Jiang, R., A. Mostafaei, J. Pauza, C. Kantzos, and A.D. Rollett, *Varied heat treatments and properties of laser powder bed printed Inconel 718.* Materials Science & Engineering A, 2019. **755**: p. 170-180.
39. Yoo, Y.S.J., T.A. Book, M.D. Sangid, and J. Kacher, *Identifying strain localization and dislocation processes in fatigued Inconel 718 manufactured from selective laser melting.* Materials Science & Engineering A, 2018. **724**: p. 444-451.
40. Blackwell, P.L., *The mechanical and microstructural characteristics of laser-deposited IN718.* Journal of Materials Processing Technology, 2005. **170**(1): p. 240-246.
41. Zhao, Y., Q. Guo, Z. Ma, and L. Yu, *Comparative study on the microstructure evolution of selective laser melted and wrought IN718 superalloy during subsequent heat treatment process and its effect on mechanical properties.* Materials Science and Engineering: A, 2020. **791**: p. 139735.
42. Reed, R.C., *The superalloys: fundamentals and applications*, ed. R.C. Reed. 2006, Cambridge (UK): Cambridge University Press.
43. Xu, Z., L. Cao, Q. Zhu, C. Guo, X. Li, X. Hu, and Z. Yu, *Creep property of Inconel 718 superalloy produced by selective laser melting compared to forging.* Materials Science and Engineering: A, 2020. **794**: p. 139947.
44. Huang, W., J. Yang, H. Yang, G. Jing, Z. Wang, and X. Zeng, *Heat treatment of Inconel 718 produced by selective laser melting: Microstructure and mechanical properties.* Materials Science and Engineering A, 2019. **750**: p. 98-107.
45. Yeh, A.-C., K.-W. Lu, C.-M. Kuo, H.-Y. Bor, and C.-N. Wei, *Effect of serrated grain boundaries on the creep property of Inconel 718 superalloy.* Materials Science and Engineering: A, 2011. **530**: p. 525-529.
46. Xiao, H., P. Xie, M. Cheng, and L. Song, *Enhancing mechanical properties of quasi-continuous-wave laser additive manufactured Inconel 718 through controlling the niobium-rich precipitates.* Additive Manufacturing, 2020. **34**: p. 101278.
47. Schirra, J.J., R.H. Caless, and R.W. Hatala, *The effect of Laves phases on the mechanical properties of wrought and cast +HIP Inconel 718*, in *Superalloys 718,625 and Various Derivatives*, E.A. Loria, Editor. 1991, The Minerals, Metals & Materials Society. p. 375-388.
48. Aydinöz, M.E., F. Brenne, M. Schaper, C. Schaak, W. Tillmann, J. Nellesen, and T. Niendorf, *On the microstructural and mechanical properties of post-treated additively manufactured Inconel 718 superalloy under quasi-static and cyclic loading.* Materials Science and Engineering: A, 2016. **669**: p. 246-258.
49. Gribbin, S., J. Bicknell, L. Jorgensen, I. Tsukrov, and M. Knezevic, *Low cycle fatigue behavior of direct metal laser sintered Inconel alloy 718.* International Journal of Fatigue, 2016. **93**: p. 156-167.
50. Cocks, A.C.F., *The nucleation and growth of voids in a material containing a distribution of grain-boundary particles.* Acta Metallurgica, 1985. **33**(1): p. 129-137.
51. Sui, S., H. Tan, J. Chen, C. Zhong, Z. Li, W. Fan, A. Gasser, and W. Huang, *The influence of Laves phases on the room temperature tensile properties of Inconel 718 fabricated by powder feeding laser additive manufacturing.* Acta Materialia, 2019. **164**: p. 413-427.
52. Sui, S., J. Chen, Z. Li, H. Li, X. Zhao, and H. Tan, *Investigation of dissolution behavior of laves phase in inconel 718 fabricated by laser directed energy deposition.* Additive Manufacturing, 2020. **32**: p. 101055.

53. Kuo, Y.-L., S. Horikawa, and K. Kakehi, *Effects of build direction and heat treatment on creep properties of Ni-base superalloy built up by additive manufacturing.* Scripta Materialia, 2017. **129**: p. 74-78.
54. Hovig, E.W., A.S. Azar, F. Grytten, K. Sørby, and E. Andreassen, *Determination of Anisotropic Mechanical Properties for Materials Processed by Laser Powder Bed Fusion.* Advances in Materials Science and Engineering, 2018. **2018**.
55. Ni, M., C. Chen, X. Wang, P. Wang, R. Li, X. Zhang, and K. Zhou, *Anisotropic tensile behavior of in situ precipitation strengthened Inconel 718 fabricated by additive manufacturing.* Materials Science and Engineering: A, 2017. **701**: p. 344-351.
56. Li, Y., K. Chen, R.L. Narayan, U. Ramamurty, Y. Wang, J. Long, N. Tamura, and X. Zhou, *Multi-scale microstructural investigation of a laser 3D printed Ni-based superalloy.* Additive Manufacturing, 2020: p. 101220.
57. Ahmad, M., R. Ignacio Picazo, B. Vladimir, J. Mohammad, and M. Mamoun, *Structure, Texture and Phases in 3D Printed IN718 Alloy Subjected to Homogenization and HIP Treatments.* Metals, 2017. **7**(6): p. 196.
58. Choi, J.-P., G.-H. Shin, S. Yang, D.-Y. Yang, J.-S. Lee, M. Brochu, and J.-H. Yu, *Densification and microstructural investigation of Inconel 718 parts fabricated by selective laser melting.* Powder Technology, 2017. **310**: p. 60-66.
59. Wang, D., C. Song, Y. Yang, and Y. Bai, *Investigation of crystal growth mechanism during selective laser melting and mechanical property characterization of 316L stainless steel parts.* Materials & Design, 2016. **100**: p. 291-299.
60. Holland, S., X. Wang, X.Y. Fang, Y.B. Guo, F. Yan, and L. Li, *Grain boundary network evolution in Inconel 718 from selective laser melting to heat treatment.* Materials Science and Engineering: A, 2018. **725**: p. 406-418.
61. Parimi, L.L., G.A. Ravi, D. Clark, and M.M. Attallah, *Microstructural and texture development in direct laser fabricated IN718.* Materials Characterization, 2014. **89**: p. 102-111.
62. Khairallah, S.A., A.T. Anderson, A. Rubenchik, and W.E. King, *Laser powder-bed fusion additive manufacturing: Physics of complex melt flow and formation mechanisms of pores, spatter, and denudation zones.* Acta Materialia, 2016. **108**(C): p. 36-45.
63. Mancisidor, A.M., F. Garciandia, M.S. Sebastian, P. Álvarez, J. Díaz, and I. Unanue, *Reduction of the Residual Porosity in Parts Manufactured by Selective Laser Melting Using Skywriting and High Focus Offset Strategies.* Physics Procedia, 2016. **83**: p. 864-873.